Deterministic Modeling for Radiation Attenuation-integrated Radon Transform in Emission Computed Tomography: Algorithm, Curve Fitting Analysis, and Introduction of Attenuation Hadamard Matrix

Mohsen Qutbi

Department of Nuclear Medicine, School of Medicine, Shahid Beheshti University of Medical Sciences, Tehran, Iran

Abstract

Purpose: The purpose of the study is to propose an algorithm to implement and visualize radiation attenuation-integrated Radon transform based on Beer–Lambert law during emission computed tomography simulation using a deterministic model and also to perform image analysis on resulting images. **Methods:** Two types of phantoms are designed: plain-disk phantom and patterned-disk phantom. The large disk is filled with an activity of 5 units and the smaller disks have 10 units of activity of ^{99m}Tc isotope as an emission map. Three transmission maps for patterned-disk phantom are created with uniform linear attenuation coefficient. Phantoms are scanned with 360° and 180° acquisition arcs. Then, using the algorithm designed, the exponential Radon transform is implemented. After that, the projections are back-projected and filtered to generate tomographic slices. Finally, all slices are analyzed using profile plotting and curve fitting. Moreover, an attenuation Hadamard matrix is provided to facilitate attenuation modeling. **Results:** The uniform intensity of activity in the phantoms is converted to a disk with progressively decreasing intensity from the periphery to the center in the tomographic slices. Similarly, the circles positioned more centrally appear less intense than those positioned in the periphery, despite all circles having equal activity. When the phantom is scanned in 180° arc, the circles closest to the camera are visualized more intensely. The profile curves of the slices generated by exponential Radon transformation are depicted as U-shaped in profile plotting and are fitted to a bi-exponential function with a near-perfect precision. **Conclusions:** The incorporation of radiation attenuation results in the development of more realistic models for quantification purposes.

Keywords: Attenuation, Beer-Lambert law, emission computed tomography, exponential, radon transform

INTRODUCTION

Single-photon emission computed tomography (SPECT) and positron emission tomography (PET) are available imaging modalities in clinical nuclear medicine. In computed tomography (CT), X-rays generated in the source (X-ray tube) are traversed through the object and then received by the detector. Conversely, in emission tomography, gamma rays emitted from inside the object are detected by the camera and then recorded in two-dimensional (2D) matrices named projections. Afterward, the projections acquired over several angles or views around the object are used for the tomographic reconstruction procedure. Several algorithms have been developed for tomographic image reconstruction that are commercially available in dedicated software platforms in nuclear medicine laboratories. From the physical perspective, gamma rays produced from the disintegration of radioactive isotopes inside the object undergo an attenuation process while traversing the physical media, for example, the patient's body, before being detected by the camera.[1,2] For this reason, SPECT and PET images are usually corrected for attenuation using computer algorithms, including Chang's method[3,4] or a transmission image obtained by

Address for correspondence: Dr. Mohsen Qutbi,
Department of Nuclear Medicine, Taleghani Hospital, Yaman St., Velenjak,
Tehran 1985711151, Iran.
E-mail: mohsen.qutbi@gmail.com, mohsen.qutbi@sbmu.ac.ir

CT component of the SPECT/CT or PET/CT cameras[5,6] to provide a more realistic estimate of the true distribution of radioactivity in the object.

Forward projection is the first step in CT that provides sinograms. This process converts a three-dimensional distribution into a 2D one using the algorithm of Radon transformation. Radon transform is a mathematical process that is constructed by line integrals of the mathematical function representing the intensity distribution of the object at different angles spanning the object. Specifically in medical imaging involving ionizing radiation, the line integrals have to be modified based on physical processes as a result of radiation-matter interaction, including attenuation and scatter. The particular modifications for X-ray transmission scanning are well defined, i.e., exponential or attenuated Radon transform according to Beer–Lambert law.[7-9] However, in emission scanning, as those in nuclear medicine, which involves emitting gamma rays from sources of activity in the object (or patient under imaging), the profile is to some extent different. The most distinct feature is that based on the location of the object, or equivalently source-to-detector distance, rays traverse tissues with different amounts of thickness and attenuation coefficient at a particular angle during Radon transform or forward projection. This fact is true for rays emanating from a specific source in the body when detecting and measuring across different angles. More notably, this issue makes the angular span of scanning an important factor. Hence, the results of 360° and 180° scans are different as a consequence of different attenuation profiles. In other words, the data in the second half of 360° arc is not redundant. Therefore, it requires relevant modification in the equations defining the Radon transform. Owing to the stochastic nature of the interaction of radiation with matter, the model can be grossly described and approximated by a simple equation of Beer–Lambert law. Therefore, for the sake of simplicity of the simulation experiments and reducing computational load, the model can be approximated to an acceptable level by a deterministic one.

The algorithm for radiation attenuation-integrated Radon transform, which considers attenuation modeling in simulation experiments in nuclear medicine, is not available in commercial image processing software packages or image processing toolboxes as a built-in or embedded function that can be used for forward projection during tomographic reconstruction. In this study, it is intended to propose an algorithm to implement radiation attenuation-integrated Radon transform based on Beer–Lambert law during emission tomography simulation experiments using a deterministic model and also to perform image analysis (including profile plotting and curve fitting) to characterize the resulting tomographic images. In addition, a new method named "attenuation Hadamard matrix" (AHM) is introduced to facilitate the process of radiation attenuation-integrated Radon transform.

METHODS

Mathematical formulation and algorithm

Based on Beer–Lambert's law, gamma photons are attenuated by interacting with the absorbent material through several physical processes. The attenuation process is modeled mathematically as follows:

$$I_{att} = I_{in}.\exp(-\mu x) \qquad \text{\{Equation 1\}}$$

where I_{in} and I_{att} are incidents and attenuated intensities of the photons, respectively. The μ and x represent the linear attenuation coefficient and the thickness of the absorbent. When the μ is not homogeneous, the model can be generalized to:

$$I_\theta^{out}(s) = I_\theta^{in}(s).\exp\left(-\int_L \mu(x,y).dl\right) \qquad \text{\{Equation 2\}}$$

where $\mu(x, y)$ is the function representing the linear attenuation coefficient of the object integrated over a line of response. I_θ^{in} and I_θ^{out} are input and output intensities at angle θ, respectively. Moreover, s is the spatial distance from the center of projection. The line of response L is a fixed distance between the X-ray generator and the detector. For modeling emission CT (ECT), the above formula is modified as follows:

$$I_\theta^{out}(s) = I_\theta^{source}(s).\exp\left(-\int_L \mu(x,y).dl'\right) \qquad \text{\{Equation 3\}}$$

Again, I_θ^{source} and I_θ^{out} are source and output intensities at angle θ, respectively. The line of response L' is a varying distance between the gamma-ray source inside the body and the detector.

In a discrete version as that in digital imaging, the field of imaging is considered as a matrix of pixels with small enough dimensions. Hence that the formula and the algorithm can be accordingly changed to:

$$I_{att} = I_{in}.\exp\left(-\sum_i \mu_i.dx\right) \qquad \text{\{Equation 4\}}$$

$$I_\theta^{out}(l) = \sum_{m=1}^M \left(I_\theta^{source}(m,l).\exp\left(-\sum_{i=m}^M \mu_i.\Delta x\right)\right) \qquad \text{\{Equation 5\}}$$

where Δx is the dimension of each pixel. For each source in each pixel, the μ is multiplied by Δx and is summed over the rows (i) of the matrix at the specific angle of θ. For the source in the first row ($m = 1$) and first column ($l = 1$), the process is done from i from 1 to M (last row) and is multiplied by the intensity of the pixels at that location (or I [m, l]). Similarly, for the second row ($m = 2$), the summation is done from $i = 2$ to M. This procedure is repeated for all rows. Finally, the output intensity is the sum of intensities from row 1 to M, which is the output intensity of a specific column (l) at a specific angle. This procedure is done for all columns of the matrix. Then, a rotation of $\theta°$ is performed, and the process is repeated from $\theta = 0$ to $\theta = \Theta$ (acquisition arc of $\theta \in [0,\Theta]$). The result is placed in the first column of the sinogram (a matrix with rows and columns equal to the number of columns of the object matrix and the number of angular samples).[10,11] The above algorithm can be rewritten as below:

$$Sinogram_\theta(l) =$$

$$\sum_{m=1}^{M}\left(\frac{Emission_\theta(m,l).}{\exp\left(-\sum_{i=m}^{M}Transmission_i.PixelSize\right)}\right) \quad \{\text{Equation 6}\}$$

Finally, the output of Beer–Lambert law or exponential radon transform (attenuation modeled sinogram) is inserted into the tomographic reconstruction process using a filtered back projection algorithm. Each sinogram is Fourier-transformed (into frequency domain) and then is multiplied by the windowed ramp filter (Hanning function as a window or a low-pass filter and ramp filter to decrease the blurring effect produced by the back projection process) [Figure 1]. After that, the filtered Fourier-transformed sinograms are back-transformed into the real or spatial domain. This procedure is repeated for the sinograms of all phantoms. For interpolation during back projection, the "bi-cubic" method is applied.[12]

Phantoms

Two types of phantoms are designed in the present study. The first type of phantom (plain-disk phantom) is a large disk filled uniformly with an activity of 5 units of ^{99m}Tc isotope with gamma rays of 140 keV and a radius of 166.4 mm as the emission map. The energy of 140 keV is used for attenuation of the gamma rays according to different tissues, as demonstrated explicitly in equation 1. Three transmission maps are designed in a way that an identical disk with the same radius is generated, each with three different values linear attenuation coefficients ($\mu_{disk1} = 0.05$, $\mu_{disk2} = 0.1$, and $\mu_{disk3} = 0.2$ cm^{-1}). The second type of phantom (patterned-disk phantom) is a similar disk-shaped object as the previous one but with 13 equally-spaced smaller disks arranged in a square-shaped pattern, simulating rods. The radii of the large and smaller disks are 166.4 mm and 16.6 mm, respectively. The large disk is filled with an activity of 5 units and the smaller disks have 10 units of activity of ^{99m}Tc isotope as an emission map (activity or intensity ratio of 2). Again, similar to the plain-disk phantom, three transmission maps for patterned-disk phantom are created with uniform linear attenuation coefficient ($\mu_{disk1} = 0.05$, $\mu_{disk2} = 0.1$, and $\mu_{disk3} = 0.2$ cm^{-1}). This pattern of transmission image represents a phantom of heterogeneous composition. Emission and transmission maps of the plain-disk or patterned-disk phantoms are presented in Figure 2. The smaller disks simulated hot spots in the large object.

Image acquisition

The matrix size for all simulations is considered 256×256 ($n = 256$) and a field-of-view of 500 mm of the camera, thus obtaining a pixel size of 1.95 mm (by the following formula: Pixel size = field-of-view/matrix size). Plain-disk phantoms are scanned with an arc of 360° and the patterned-disk phantoms are scanned twice with acquisition arcs of 360° and 180°. An angular sampling of 1° is used for image acquisition.

Profile plotting and curve fitting analysis

Tomographic slices generated are visualized in a grayscale map. All tomographic images are minimum–maximum normalized in a way that the minimum and maximum values are set to the interval of 0–1. Intensity profiles of activity distribution of each group of phantoms are plotted separately
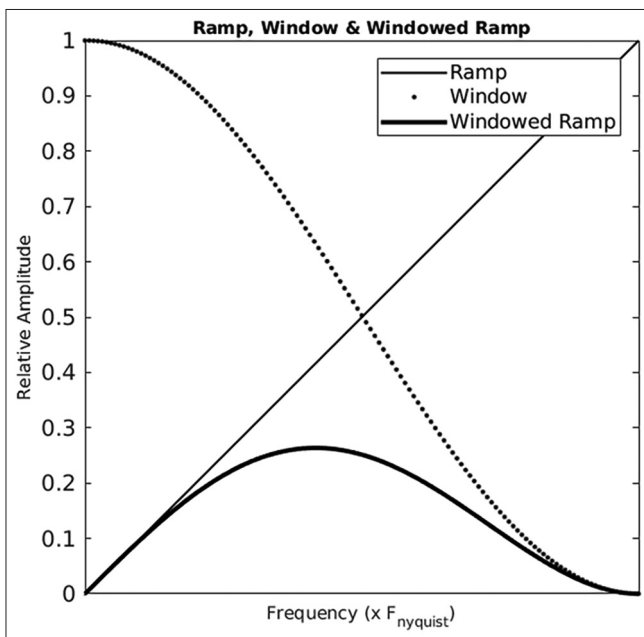
Figure 1: Diagram of the windowed ramp filter in the frequency domain. The x-axis indicates the relative frequency (as a ratio of Nyquist Frequency) and the y-axis indicates the relative amplitude of the frequency components in the image
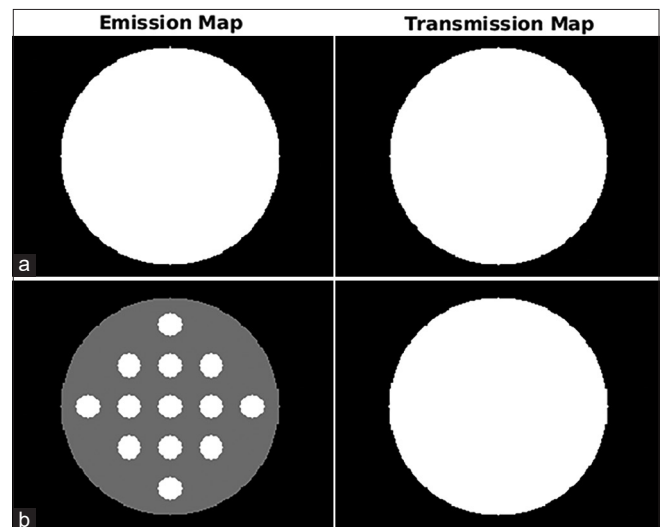
Figure 2: (a) Emission (left) and transmission (right) maps of the plain-disk phantom. Both are scales separately. (b) Emission (left) and transmission (right) maps of the patterned-disk phantom. In the emission maps, 13 equally-spaced smaller disks are arranged in a diamond-shaped pattern, with equal intensity but higher than that of the background. The transmission map of the phantom is, in contrast, uniform. No difference exists in the attenuation coefficient of small and large objects

and are compared. The intensity profiles of the plain-disk phantom with different values of linear attenuation coefficient are fitted to a bi-exponential model using the following formula:

$$f(x) = ae^{bx} + ce^{dx} \qquad \{Equation\ 7\}$$

Where, a, b, c, and d are the coefficients obtained from the optimization process with the method of nonlinear least square and the algorithm of Trust-Region. X represents distance or pixel number and f (x) is the pixel value or intensity. Furthermore, indices of the goodness of fit are also calculated. The indices are summed square error (SSE), root-mean-squared error (RMSE), R-squared, and adjusted R-squared. This procedure is repeated for each value of the attenuation coefficient.

Attenuation Hadamard matrix

The term, $\exp\left(-\sum_i \mu_i.\Delta x\right)$ in Equation 4, plays the role of attenuation profile of each point (or pixel) in the object when detected by the camera. This term is computed from the transmission or μ map obtained from the phantom or object. Thus, by calculating this factor, and then element-wise multiplying to the original distribution or emission map, the attenuation-modeled ECT can be obtained. For generating sinograms and back-projected tomographic slices, two following equations are used, respectively;

$$M(s,\theta) = \exp\left(+\Sigma_i \mu_i.\Delta x\right) \qquad \{Equation\ 8\}$$

and,

$$AHM(x,y) = \sum_{\theta=0}^{2\pi} M(s,\theta) \qquad \{Equation\ 9\}$$

Here, the inverse of this matrix (AHM) is multiplied point-by-point or element-by-element to the matrix, demonstrating the activity distribution in the object or phantom as below. The operator ⊙ denotes the Hadamard product or multiplication of two matrices.[13]

$$I_{attenuated} = I_{source} \ "\ 1/AHM \qquad \{Equation\ 10\}$$

To achieve the attenuated Radon transform with less computation load. For this experiment, two phantoms are created. One is a patterned-disk phantom the same as above and another is a more complex phantom of the human thorax (including the objects of heart, liver, and thoracic wall). The image acquisition from emission images is obtained as mentioned above. And then, from transmission images, AHM image is generated by creating related sinograms and tomographic reconstruction using the above algorithm.

Implementation

All the computations for image processing and visualization are conducted in the MATLAB software package (The MathWorks Inc., version 2021b under Linux). The specifications of the computer used are Intel® Core™ i7–10870H (up to 4.5 GHz, 8 cores, and 16 threads) CPU and 32GB RAM.

RESULTS

In Figure 3, tomographic slices of plain-disk and patterned-disk phantoms are shown. The first row belongs to the scan with 360° arc. In the scan without incorporating the attenuation
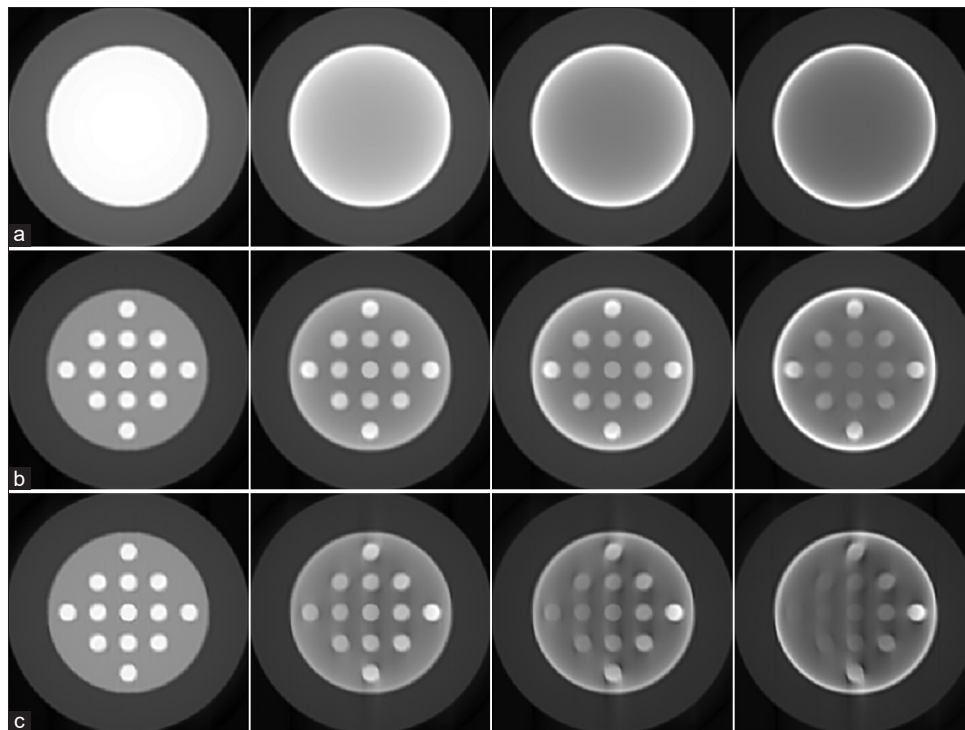

Figure 3: (a) (From left to right) tomographic slice of the phantom without and with incorporation of attenuation for $\mu_{disk1} = 0.05$, $\mu_{disk2} = 0.1$, and $\mu_{disk3} = 0.2\ cm^{-1}$. The same applies to patterned-disk phantom imaged with 360° (b) And 180° (c) Acquisition arcs

model, i.e., using a simple Radon transform, the disk appears uniform from periphery to center. However, as can be seen in the other three images, the uniform intensity of activity in the phantom is converted to disk with progressively decreasing intensity from the periphery to the center. As the µ of the phantom increases, the periphery-center gradient becomes steeper and steeper. This radial gradient is constant circumferentially over all angles. The images in the second row demonstrate the 360° scanning of the patterned-disk phantom. The leftmost image is scanning without attenuation and the other three ones, as mentioned earlier, belong to scanning incorporating attenuation modeling in phantoms with three different values of µ. Similarly, the circles positioned more centrally appear less intense than those positioned in the periphery despite all circles having equal activity. When the phantom is scanned in 180° arc, the circles closest to the camera are visualized as more intensely and those in more distance, even in the periphery of the phantom, are seen as less active.

Normalized intensity profiles of the phantoms and related tomographic slices are demonstrated in Figure 4. For plain-disk phantom (a), The profile drawn diametrically is a straight line and the profile curve of the nonattenuated slice follows closely from the center to the periphery. In contrast, the curves of the slices generated by exponential Radon transformation, are depicted as U-shaped. The more the µ of the phantom, the deeper the curve in the center. The plot of the intensity profile of the patterned-disk phantom (b) Demonstrates similar findings as in A. Bi-exponential curve fitting for the plain-disk phantom with different values of µ is plotted [Figure 5]. As can be seen, the curve fitted to the data of the phantom with µ = 0.05 is less steep compared to the phantom with µ = 0.2 that is steeper. Moreover, the curve of the phantom with µ = 0.1 is in between.

In Figure 6a, the activity and µ maps of patterned-disk phantom and corresponding sinograms and tomographic slices with and without considering radiation attenuation during the Radon transform are presented. Similarly, in Figure 6b, the emission (activity) and transmission (µ) maps of the thorax phantom and corresponding sinograms and tomographic slices are provided. Figure 7 demonstrates the images of AHM and the inverse of AHM and their corresponding attenuated tomographic slices calculated by division and multiplication of emission image by inverse of AHM and AHM are provided for both patterned-disk phantom and thorax phantom.
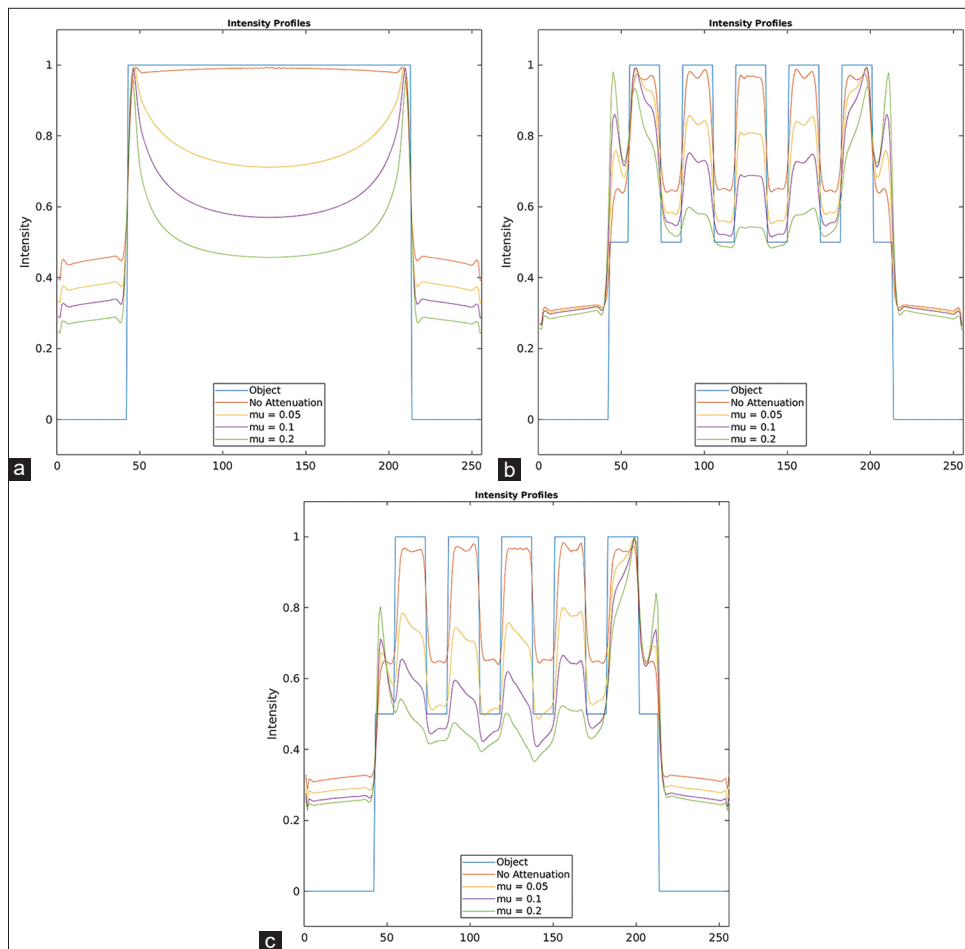

Figure 4: Intensity profile plots of a tomographic slice of plain-disk phantom (a) And patterned-disk phantom imaged with 360° (b) And 180° (c) Acquisition arcs. The horizontal axis indicates the distance or pixel number across the related images and the vertical axis denotes the normalized intensity of pixels (values between 0 and 1)

DISCUSSION

In ECT, radiation emitted from the interior of the object undergoes an attenuation process during forward projection or Radon transform. Then, by tomographic reconstruction, pixels that are distant from the camera or located in objects with a higher attenuation coefficient do not demonstrate the true intensity or activity uptake. Many significant efforts have been made so far to compensate for the effect of attenuation by means of various algorithms. However, in some circumstances, modeling of this phenomenon (radiation attenuation during Radon transform) may be of interest during simulation experiments of ECT. Monte Carlo simulation, which is based on the randomness and stochastic nature of the radiation-matter interaction and radioactive

decay process, performs nearly perfectly for this purpose. However, it requires a lengthy and cumbersome computation. Deterministic modeling of radiation attenuation provides acceptable results.[1,2,7-9]

The incorporation of radiation attenuation as one of the main physical processes involved in the interaction of gamma photons with the matter based on Beer–Lambert law results in the development of more realistic models for quantification purposes. Using exponential or attenuation-modeled Radon transform in emission tomography enables researchers to evaluate the effect of attenuation in nuclear medicine imaging. Modeling the phenomenon of radiation in emission tomographic images is different from that of transmission tomographic images since the source is inside the object and the line integrals or ray sums are different. In this study, we designed and developed a phantom with both emission and transmission maps. The transmission map is used as the image provided by the CT scanner for attenuation modeling of gamma rays in the emission image. According to the Beer–Lambert law, the ionizing photons are attenuated exponentially by matter. In addition to visualization of the effect of attenuation tomographic images, we plotted the intensity profile of the slices shown in Figure 4 that were concordant with the so-called exponential pattern. As can be seen from tomographic slices, by increasing the value of μ, the deeper or more central parts of the object which are more distant from the camera, are attenuated to a higher extent. This pattern is also visible in the images of patterned-disk phantom. More central smaller disks are attenuated higher than those that are located more peripheral. Another finding which is worth mentioning is the modeling of the attenuation in the setting of imaging acquired with 180° arc. Interestingly, in image acquisition with 180° arc, even peripheral small disks that are distant from the camera are attenuated profoundly. This finding emphasizes that in the radiation attenuation-modeled Radon transform, no redundancy of data exists in the second half of 360°
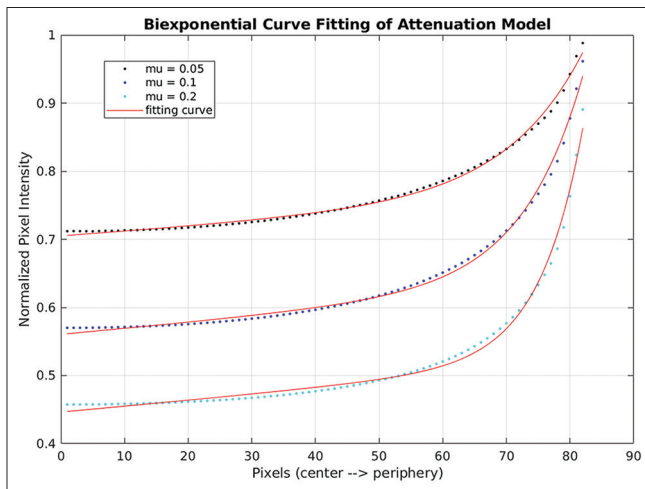
Figure 5: Plot of curve fitting analysis of the tomographic images of the plain-disk phantom with three different values of linear attenuation coefficient. The data of each one is fitted to a bi-exponential model. The data extracted are the profile of the image of the object from the center to the edge of the object. The horizontal axis indicates the distance or pixel number across the related image and the vertical axis denotes the normalized intensity of pixels (values between 0 and 1)
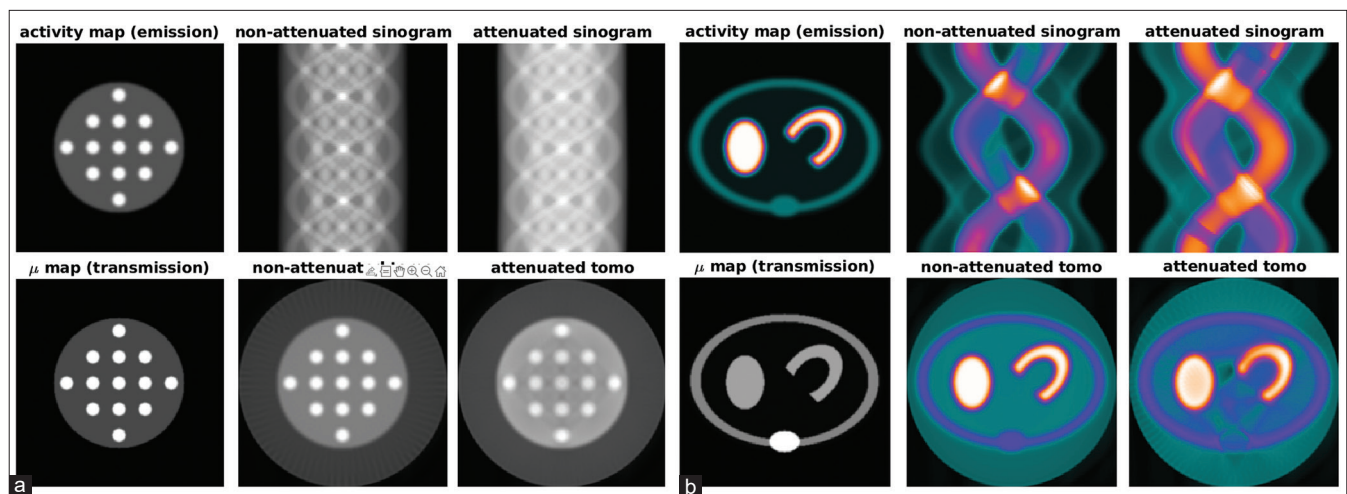
Figure 6: The activity and μ maps of patterned-disk phantom and corresponding sinograms and tomographic slices with and without considering radiation attenuation during Radon transform for patterned disk (a) and thorax (b) Phantoms
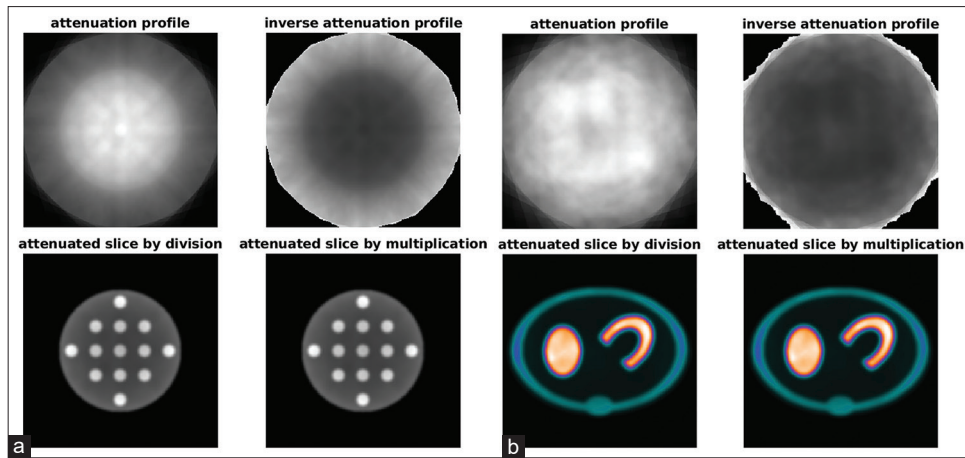
Figure 7: Images of attenuation Hadamard matrix (AHM) and the inverse of AHM and their corresponding attenuated tomographic slices for patterned-disk (a) And thorax (b) Phantoms

Table 1: The results of curve fitting with bi-exponential function for plain-disk phantoms with different values of linear attenuation coefficient (μ)

	Plain-disk phantoms		
	$\mu=0.05$	$\mu=0.1$	$\mu=0.2$
Coefficients (with 95% CI)			
a	0.7339 (0.7305–0.7372)	0.5977 (0.5945–0.6008)	0.4835 (0.4808–0.4861)
b	0.0232 (0.0191–0.0272)	0.0368 (0.0314–0.0422)	0.0457 (0.0393–0.0521)
c	0.0073 (0.0053–0.0094)	0.0042 (0.0029–0.0055)	0.0008 (0.0005–0.0012)
d	1.97 (1.817–2.124)	2.508 (2.336–2.68)	3.505 (3.257–3.753)
Goodness of fit			
SSE	0.0014	0.0028	0.0044
RMSE	0.0042	0.0060	0.0075
R^2	0.9960	0.9953	0.9924
Adjusted R^2	0.9959	0.9951	0.9921

SSE: Summed squared error, RMSE: Root mean squared error, CI: Confidence interval

acquisition arc in contrast to the general form of the Radon transform.

By curve fitting analysis [Figure 5], the profile plots were fitted to a bi-exponential function by near-perfect precision. The procedures are done for three different linear attenuation coefficients. As expected, the higher the value of the coefficient, the steeper the exponential curve as the profile plot. The indices of the goodness of fit, SSE, and RMSE were close to zero and the R-squared and adjusted R-squared were higher than 99% available in Table 1. By this means, we could show that the effect of radiation attenuation in tomographic slices can be accurately modeled by a bi-exponential mathematical function. Moreover, the computations required for the procedure of exponential Radon transform can be performed on a computer with a medium level of hardware at a reasonable time.

In this project, a new simple technique for modeling radiation attenuation in ECT is proposed and introduced, by which the procedure is much less cumbersome. At first, a matrix of attenuation profile is constructed by the equations 8, 9, and 10 (or transmission or μ map), then, the status

and the extent of attenuation of each pixel are computed. After that, by pixel-by-pixel multiplication (Hadamard product)[13] of the emission map of the phantom to this matrix, the radiation attenuation modeled tomographic slices are formed.

CONCLUSIONS

Although the nature of the physical attenuation of radiation is inherently random or stochastic, the phenomenon can be grossly approximated by a deterministic model using the formula of Beer–Lambert law. This kind of modeling bears a remarkably lower computation load compared to Monte Carlo simulations and modeling. Hence, these methods can be utilized in image processing tasks, including tomographic reconstruction. Despite all these facts, the gold standard method is stochastic modeling for such experiments.

Conflicts of interest
There are no conflicts of interest.

REFERENCES

1. International Atomic Energy Agency. Nuclear Medicine Physics. Vienna: IAEA; 2015.
2. International Atomic Energy Agency. Diagnostic Radiology Physics. Vienna: IAEA; 2014.
3. Chang LT. A method for attenuation correction in radionuclide computed tomography. IEEE Trans Nucl Sci 1978;25:638-43.
4. Saha K, Hoyt SC, Murray BM. Application of Chang's attenuation correction technique for single-photon emission computed tomography partial angle acquisition of Jaszczak phantom. J Med Phys 2016;41:29-33.
5. Zaidi H, Hasegawa B. Determination of the attenuation map in emission tomography. J Nucl Med 2003;44:291-315.
6. Dickson JC, Armstrong IS, Gabiña PM, Denis-Bacelar AM, Krizsan AK, Gear JM, *et al.* EANM practice guideline for quantitative SPECT-CT. Eur J Nucl Med Mol Imaging 2023;50:980-95.
7. Kim KI, Tewarson RP, Bizais Y, Rowe RW. Inversion for the attenuated radon transform with constant attenuation. IEEE Trans Nucl Sci 1984;31:538-42.
8. Bal G. On the attenuated Radon transform with full and partial measurements. Inverse Probl 2004;20:399-418.
9. Tretiak O, Metz C. The exponential radon transform. SIAM J Appl Math 1980;39:341-54.
10. Figal M. CT Reconstruction. In: Birkfellner W, editor. Applied Medical Image Processing: A Basic Course. New York: CRC Press; 2014. p. 339-70.
11. Hansen PC, Jørgensen JS, Lionheart WR. Computed Tomography: Algorithms, Insight, and Just Enough Theory (Fundamentals of Algorithms). Philadelphia: SIAM – Society for Industrial and Applied Mathematics; 2021.
12. Zeng GL. Image Reconstruction: Applications in Medical Sciences. Berlin/Boston: Walter de Gruyter GmbH; 2017.
13. Styan GPH. Hadamard products and multivariate statistical analysis. Linear Algebra Appl 1973;6:217-24.